1300 nm Semiconductor Optical Amplifier Compatible With an InP Monolithic Active/Passive Integration Technology

Joel Hazan, Stefanos Andreou, Dzmitry Pustakhod, Steven Kleijn, Kevin A. Williams, and Erwin A. J. M. Bente

***Abstract*—In monolithic photonic integrated circuits (PICs), an optimized active/passive integration is needed to provide efficient coupling and low amount of interface reflections between amplifiers and passive components. A 1300 nm semiconductor optical amplifier (SOA) on InP substrate and optimized for butt-joint reflections is investigated. Material performance were assessed from measurements of broad area lasers. Room temperature operation reveals 1.2 W single facet output power with threshold current around 100 A/cm^2 per well. Characteristic temperatures of $T_0 = 75$ K and $T_1 = 294$ K were obtained. A compact model description of the SOA, suitable for the design of PICs and rate equation analysis, was applied to parametrize the unsaturated gain measurements. Current injection efficiency of 0.65, transparency carrier density of 0.57 10^{18} cm^{-3}, and free carrier absorption losses up to 15 cm^{-1} were extracted from fitting the data. The model is verified with measurements of optical gain saturation. A modal gain of 15 dB for a 600 μm long narrow ridge SOA leads to output saturation power higher than 30 mW at 7 kA/cm^2. This building block contributes to the development of an InP monolithic integration technology in the 1300 nm range, which can enable the use of photonic integrated circuits in many kind of applications.**

***Index Terms*—InP, monolithic integrated circuits, o-band telecommunications, semiconductor optical amplifiers, semiconductor device modeling.**

I. INTRODUCTION

SEMICONDUCTOR optical amplifiers (SOAs) are a critical component for numerous kinds of photonic integrated circuits (PICs). SOAs are the basis for the development of light sources such as light emitting diodes [1] and tunable laser systems [2]. These components are also used to increase output power and to maintain sufficiently high signal levels as the signal propagates throughout many optical components [3]. Extensive studies have been performed on 1300 nm SOA [4], [5], since commercial fibers present near zero dispersion in this spectral region [6]. SOAs in this wavelength range are widely used in data centers since high bit rates can be achieved without the need of dispersion compensation. O-band SOAs can then be included in more complex systems such as dual wavelength division multiplexers for high bit rate and capacity transmission systems [7]. 1300 nm SOA are commonly used for their low temperature dependence [8] and high efficiency [9], [10]. Different InP SOA were designed as discrete components and optimized for low polarization dependence [5], high operating temperatures [11] and wide gain bandwidth [12].

The introduction of active-passive integration technologies creates the opportunity of using 1300 nm SOAs in more complex circuits such as extended cavity widely tunable laser systems [13] or optical switches [14]. Both hybrid integration [15] and hetero-epitaxial growth [16] technologies at 1300 nm have been developed to integrate SOA with passive waveguide on Si substrates. Threshold current as low as 450 A/cm^2 has been reported for quantum dot laser grown on Si (001) [17]. Narrow width ridge SOA revealed gain as high as 45 cm^{-1} and on chip optical power of 25 dBm at room temperature [18]. However, these "III-V on Si" approaches face the challenge of the creation of some bonding defects at the interface between the two different materials [19].

The development of a new quantum well-based InP SOA in the 1300 nm wavelength regime is a crucial step in the development of a 1300 nm monolithic integration platform on InP. This 1300 nm platform on InP is designed to have minimized active passive interface reflections and optical loss [20] with the same integration process. Moreover, the introduction of a 1300 nm InP generic integration platform, based on the already existing one [22], brings the benefit of being able to use a standard set of building blocks to create various complex circuits and optical functionalities. The platform will allow fast and cost-effective prototyping in the 1300 nm band, giving the opportunity to serve many different applications.

In this paper, we present the design and the characterization of a new InGaAsP/InP SOA that will be integrated with a low propagation loss passive waveguide via a butt-joint integration scheme with a single regrowth step, to further develop a new monolithic generic integration technology at 1300 nm. The analysis of the fundamental properties of active devices such

Manuscript received February 18, 2022; revised May 6, 2022; accepted May 7, 2022. Date of publication May 16, 2022; date of current version June 3, 2022. This work was supported in part by the Research Program HTSM2017 through a project An Integrated Optical Coherence Tomography system for medical imaging at 1300 nm under Grant 16251 and in part by Dutch Research Council. (*Corresponding author: Joel Hazan.*)

Joel Hazan, Dzmitry Pustakhod, Kevin A. Williams, and Erwin A. J. M. Bente are with Photonic Integration Group, Electrical Engineering, Eindhoven University of Technology, Eindhoven, Den Dolech 2, 5612 AZ Eindhoven, The Netherlands (e-mail: j.hazan@tue.nl; d.pustakhod@tue.nl; k.a.williams@tue.nl; e.a.j.m.bente@tue.nl).

Stefanos Andreou and Steven Kleijn are with SMART Photonics, High Tech Campus 29, 5656 AE Eindhoven, The Netherlands (e-mail: stefanos.andreou@smartphotonics.nl; steven.kleijn@smartphotonics.nl).

Digital Object Identifier 10.1109/JPHOT.2022.3175373

as temperature and current dependent emissions reveals that the requirement of being compatible with an active/passive butt-joint integration technology does not lead to any major downgrades in the optical performance of the active layer stack chosen.

First, the active layer stack design is presented together with the considerations made to meet the requirement of compatibility with an active passive monolithic integration technology on InP at 1300 nm. Then, the overall material quality is addressed through measurements of broad area Fabry-Perot lasers and the analysis of parameters which highlight the device performance. The description of a compact model for a narrow ridge width optical amplifier is presented and verified through experimental data of gain spectra and optical gain saturation. This SOA model description can be then use in the design and simulation of photonic integrated circuits fabricated on a 1300 nm generic InP integration technology.

II. Active Layer Stack Design

To develop a generic platform for photonic integration at 1300 nm, active devices such as lasers and amplifiers need to be integrated with passive components such as propagation waveguides, splitters, and reflectors. One of the main challenges of the integration technology is to engineer the active and the passive components so that the best coupling and the lowest amount of interface reflections are ensured. In this work, an InGaAsP-based optical amplifier with photoluminescence (PL) targeted at 1310 nm, is designed, and simulated with the commercial simulator HAROLD licensed from Photon Design. In active-passive integration it is important to minimize reflections from the butt-joint active passive area transitions to at least -50 dB. The reflections can lead to poor side mode suppression inside tunable laser systems or instabilities when causing feedback to the laser. Therefore, an important requirement during the design of the active layer stack was to match the fundamental mode effective index of the SOA to that of the InP passive waveguide designed for 1300 nm light propagation. The change in the effective index with respect to the passive waveguide has been limited to $\Delta n_{eff} < 5\ 10^{-3}$ and the mode overlap has been kept to $>$99% in simulations, to keep reflections at the active passive interfaces $<$50 dB. This requirement is targeted as follows. Firstly, the total active region thickness is chosen to be 400 nm and both the separate confinement heterostructure and the barriers present a quaternary energy bandgap (Q-value) of 1.1 μm, to match the passive waveguide dimensions and composition. Inside the active region four InGaAsP based quantum wells are embedded. A low number of wells does not lead to very uneven carrier densities in the different wells and in this way, the material gain can be reasonably approximated as four times the gain arising from a single quantum well. Moreover, low number of quantum well is a good compromise between having sufficient high small signal gain and a limited modal effective index mismatch with a passive waveguide with the same geometry. The second aspect concerns the design of the quantum wells in which compressive strain is used, and the design of the barrier layers which are needed to compensate the strain. It turns out the compressive strain level that can be used in the quantum wells is limited by the requirement to maintain a sufficiently low effective index mismatch with the passive waveguide. The introduction of compressive strain leads to an increase in the transverse electric (TE) gain which is beneficial for achieving lower threshold current levels [23], [24] in lasers and improves high temperature performance [8].

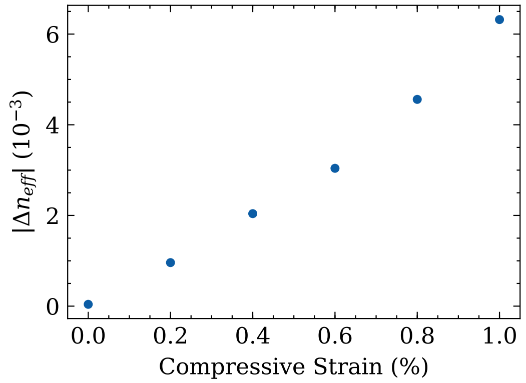

Fig. 1. Difference in the effective index of an active shallow etched ridge waveguide with respect of a passive waveguide with ridge width W $= 2$ μm as function of compressive strain applied to the quantum wells. The effective index of a 2-μm-wide passive shallow etched waveguide is 3.26.

The compressive strain removes the degeneracy in the valence sub-bands at the Γ point. The splitting of the heavy and light holes degenerate bands decreases significantly the Auger recombination and the intervalence band absorption [10], increasing the SOA optical performance. On the other hand, the introduction of strain induces a change in the refractive index of the well, and a change in the Q-value of the barriers from the targeted value (Q $= 1.1\mu$m) which can lead to an effective index change in the active region of the waveguide and a smaller mode overlap with the passive waveguide. The fundamental TE mode effective index of a straight waveguide with same single mode ridge width of 2 μm is equal to 3.26. The introduction of strain increases the effective index change with respect to a passive waveguide with the same ridge width. This is depicted in Fig. 1 which shows the calculated modal refractive index as function of different compressive strain in a four quantum well structure using HAROLD software licensed from Photon Design.

Therefore, it is possible to imply that the more the strain is the higher the effective index difference is which can increasingly deteriorate the mode overlap at the active passive interface. This will introduce higher coupling loss and strong reflections at the butt-joint interfaces which can compromise the performance of integrated laser systems. Moreover, simulations show that strain values higher than 0.8% do not noticeably increase the TE material gain. A smaller than 10% increase in the material gain occurs when the amount of compressive strain in the quantum wells is doubled in the simulation from 0.7% to 1.4%. For this reason, we limit the amount of compressive strain at 0.8%, to ensure the butt-joint reflection is smaller than -50 dB inside our extended cavity tunable laser systems. At room temperature, isothermal one-dimensional simulations of the optimized layer stack design, shown schematically in Fig. 2(a), reveal a threshold

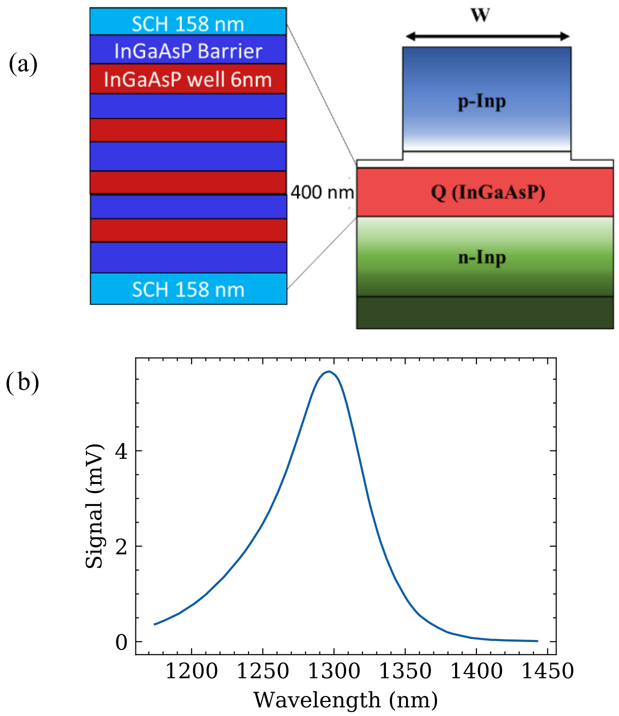

Fig. 2. (a) Cross-sectional view of the fabricated SOA acitve layer stack. (b) Measured photoluminescence spectrum of the wafer with this layer stack design.

current of 300 A/c m^2 and minimum internal loss of the amplifier as low as 4cm^{-1}. A material gain for TE polarized light of 2200 cm^{-1} is predicted at 5 kA/cm^2. Finite difference element mode simulations calculate an optical confinement of around 4% inside the active region for a shallow etched 2 μm wide ridge waveguide. This value is approximately 1% for every quantum well present inside the SOA.

III. DEVICE FABRICATION

The InP based fully active test structures were fabricated by Smart Photonics following a well-established processing technique [22]. The layers are grown on top of a heavily n-doped ($510^{18} cm^{-3}$) InP (100) substrate. The active layers are grown using Metal Organic Chemical Vapor Deposition (MOCVD). After the epitaxial growth the waveguides are defined to obtain the shallow waveguide cross section as depicted in Fig. 2(a). The waveguides are all etched using an Inductively Coupled Plasma (ICP) dry etch process. The different waveguide ridge widths are defined in a single lithography step to ensure good alignment and fabrication reproducibility. After etching, the waveguides are passivated and planarized through the deposition of a Polyimide layer. The contact and a metallization layer are applied on top and on bottom of the structure to allow current conduction. The photoluminescence signal of the four quantum well amplifier is measured using a technique described in [25]. The results, shown in Fig. 2(b), reveal that the maximum emission targeted at 1300 nm during the design phase, was achieved during the fabrication. A photoluminescence peak at 1290 nm with a 70 nm wide 3-dB bandwidth is reported in the graph measured for a 3-inch wafer.

IV. ACTIVE LAYER STACK QUALITY EVALUATION

To establish the quality of the layer stack used in the fabrication of optical amplifier first the following, generally published, parameters are determined. These results to be the transparency current density J_0, the internal quantum efficiency η_i and the amplifier internal loss α_i. It is possible to extract these parameters, using a well-established method as published in [26], [27], from the analysis of the output optical power as function of the injected current density. Since these parameters are generally independent on the geometry of the device, they could inform us on the gain material performance of a SOA at any operating temperature. These parameters can be used to compare the designed device with 1300 nm amplifiers available in literature and with the simulated device predictions. To identify the temperature dependence of these SOA parameters, it is needed to evaluate the characteristic temperatures T_0 and T_1. Those can be obtained from the analysis of the light intensity (L-I) curves at different operating temperatures as described by [28]. Higher characteristic temperatures T_0 and T_1 reflect lower temperature dependence and this indicates that the amplifiers performance deteriorates less at high operating temperatures. Differently from [28], in this work we are investigating the temperature dependence of the broad area lasers from length-independent parameters. Thus, the analysis to extract T_0 and T_1 is applied to the transparency current density J_{tr} and the internal quantum efficiency η_i and not to the threshold current J_{th} and the external quantum differential efficiency η_d as often reported in literature.

For this purpose, a set of Fabry-Perot lasers with uncoated cleaved facets and different lengths between 500 and 1200 μm, and ridge widths between 1 and 100 μm have been fabricated. The cleaved facets leave reflections of approximately 30% at both ends. These lasers have been characterized over a range of operating temperatures between 20 and 80 °C. Broad area stripes, with width of 100 μm, lasers are tested. On devices with this wide ridge area, it is possible to approximate that all the current that is going through the metallic contact is reaching the active region inside the waveguide. In this way, it is possible to neglect the effect of the ridge and measure the material property only. Pulse current measurements, with pulse width of 10 μs and 1% duty cycle (DC), are performed to avoid thermal effect inside the lasers. Measurements with shorter pulse duration reveal constant output power at current density higher than 3 kA/cm^2. We believe this is since very short pulses do not leave sufficient time to the current to flow through the contact layer into the active region. The pulsed operation L-I measurements of the broad area Fabry-Perot cavity lasers reveal high output powers and high temperature of operation. In Fig. 3(a), averaged L-I curves are shown for measurements over 10 identical devices on the same wafer for 1300 μm long amplifiers with broad area stripes. The current is swept between 0 and 5 A reaching up to 4.8 kA/cm^2 in density. We can notice the output power from a single facet of 1200 μm long devices at room temperature (T = 20 °C) goes up to 1.25 W, with standard deviation of around

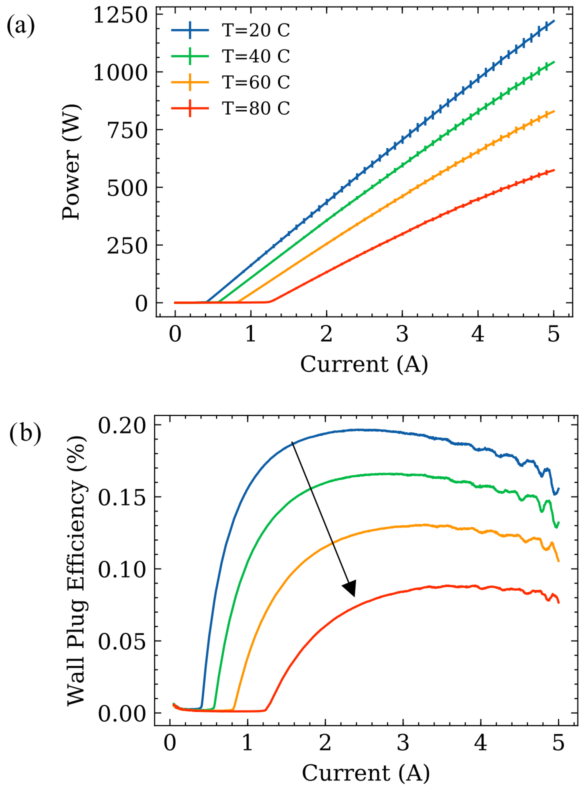

Fig. 3. (a) Total output power per facet and (b) wall plug efficiency, for a 1200 um long and 100 um wide Fabry-Perot laser at different heat sink operating temperatures. The measurements were performed using pulsed current with 10 μs of pulse duration and 1% duty cycle.

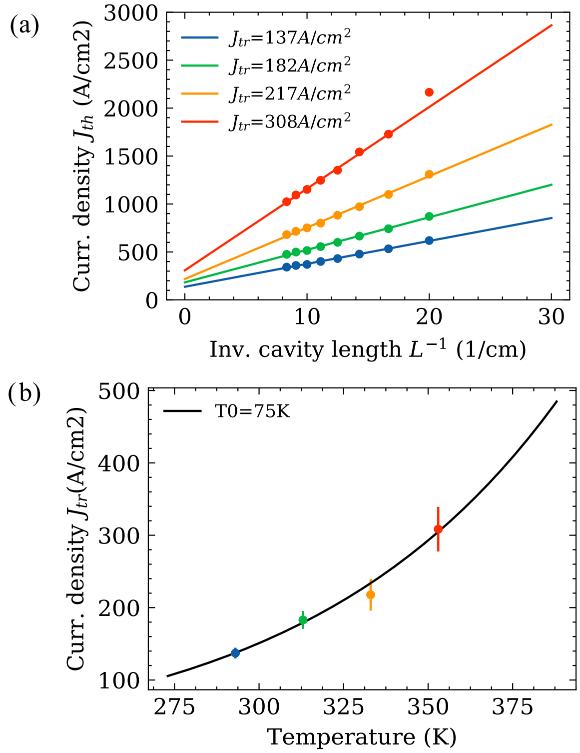

Fig. 4. (a) Threshold current density as function of inverse cavity length and linear fit to obtain $\boldsymbol{J_{tr}}$ for different heat sink T. (b) $\boldsymbol{J_{tr}}$ as function of temperature and measurement fit to obtain the characteristic temperature $\boldsymbol{T}_0 = 75$ K of broad area lasers. Legend in 3a) is also valid here.

30 mW. Threshold current density as low as 350 A/cm^2 has been measured at room temperature. The wall plug efficiency (WPE) exhibits a drop from 20% to 8% from room temperature to 80 °C, as depicted in Fig. 3(b). In Fig. 3(a) it is possible to notice that the relative change in the threshold current and in the slope of the L-I curve is constant between 20 and 60 °C. The increase in the threshold current is estimated around 10 mA/ °C, ranging from 400 up to 800 mA between 20 and 60 °C. When the substrate is set to 80 °C, it is possible to note that the stimulated emission slope is slightly lower. This can be due to the lower performance of the active material at high heat sink temperature. Moreover, at 80 °C we can notice some roll-over at around 4 A of injected current, which is due to the relatively long pulse duration of 10 μs that accumulates heat in the active region.

By measuring the threshold current density of broad area lasers of different cavity lengths, it is possible to evaluate the material without the effect of the ridge, as function of laser temperature of operation.

In Fig. 4(a) the fit of the threshold current density as function of the inverse cavity length is shown. The transparency current density is calculated as the intercept of the fit line which corresponds to an infinitely long cavity with zero reflections at the mirrors, as stated in [26]. The uncertainty over the J_{tr} parameter is given by the covariance matrix of the fit and can vary between 10% and 20%, depending on the temperature as can be seen in Fig. 4(b). The observed temperature dependency of the transparency current density shows a mean value of 140 A/cm^2 for 20 °C and around 310 A/cm^2 for 80 °C. These values, as shown in Fig. 4(b) are in accordance with those reported in [28] for III-V broad area lasers. At higher temperature, the statistical carrier distribution across the states of the quantum wells becomes broader and this results in an increase in the transparency current density due to the reduction in the differential gain [28]. From the exponential fit with equation from [28], the characteristic temperature T_0 is calculated to be 75 K, which is comparable to what found in literature for Al-based lasers on InP substrate [29].

From the stimulated emission part of the curve above threshold, it is possible to obtain the external differential efficiency η_d. The slope is determined from the threshold current up to 1 A above threshold to avoid the range where thermal roll-over occurs. Fig. 5(a) shows η_d as a function of the laser cavity length. By fitting the data to the equation in [26], the internal efficiency η_i and the scattering loss α_i are extracted. The amplifier losses are the sum of the free carrier absorption loss [11] and carrier independent loss mechanism such as photon scattering [30] or intervalence band absorption [10]. It is noticeable how at higher temperature the measurement of η_d is less accurate than the threshold current density value since the slope of the L-I curves is evaluated at higher current levels.

This leads to higher contribution of thermal effects due to the active region heating. In this way we have a much higher uncertainty over the estimation of η_i and α_i at higher operating

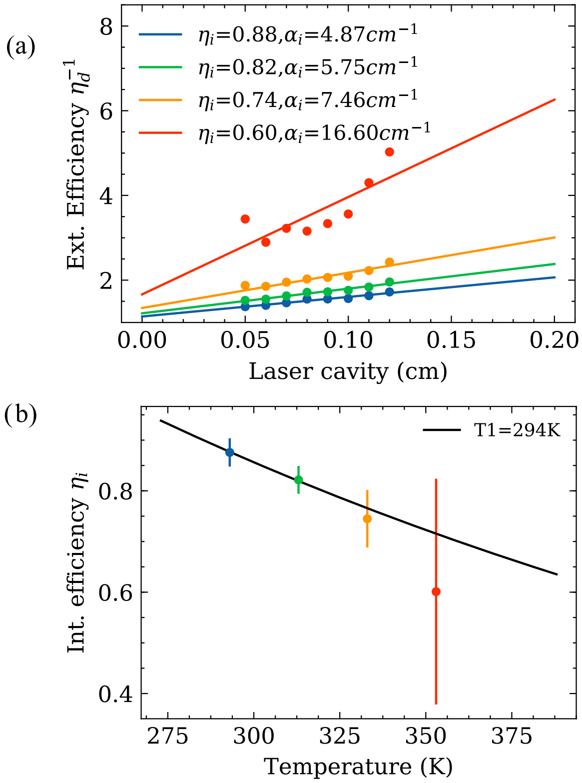

Fig. 5. (a) External differential quantum efficiency as function of laser cavity length (dots) and fit (line) from [26] to extract the injection efficiency $\boldsymbol{\eta_i}$ and the internal loss $\boldsymbol{\alpha_i}$ at different heat sink Temperature. (b) $\boldsymbol{\eta_i}$ as function of heat sink temperature and measurement fit to obtain the characteristic temperature $\boldsymbol{T_1 =}$ 294$\boldsymbol{K}$ of broad area lasers. Legend in 3a) is also valid here.

temperatures. Internal losses are increasing with the temperature due to the increase intervalence band absorption in the quantum wells [31].

They are determined to vary from 5 cm^{-1} to 16 cm^{-1} in a temperature range of 20 to 80 °C. The fitted internal efficiency as function of temperature shown in Fig. 5(b) allows to calculate the characteristic temperature $T_1 = 294$ K, which identifies the temperature dependence of the stimulated emission slope. T_1 lies in the reported 'state of the art' characteristic temperatures around 300 K for 1300 nm broad area lasers on InP substrate [29]. The measurements of Fabry-Perot broad area lasers demonstrate that the device performance agree with the one-dimensional simulations.

The amplifier internal losses were observed to be lower than 5 cm^{-1} at room temperature, as was expected from the simulation. Furthermore, the thermal dependence of the extracted parameters is very close to what is presented in literature for InP based amplifiers. This suggests that the requirement of being compatible for an active-passive butt-joint integration does not lead to major compromises in the active material performance at low carrier density values. The broad area laser analysis has been performed to establish whether or not the designed active material meets the desired specification. In the following chapter a detailed analysis of the performance of single mode ridge width SOA, will be addressed together with a compact model to include into laser circuits. Before that the study of J_{tr} as function of the amplifier ridge width, shows how the ridge width affects the SOA parameters.

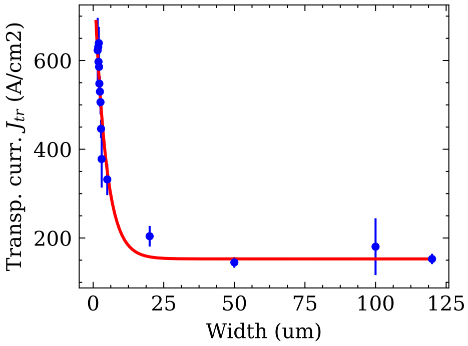

Fig. 6. Measured (blue dots) transparency current density as function of waveguide ridge width, together with an exponential fit (red line) of $\boldsymbol{e^{-W/L_d}}$ where a carrier diffusion length $\boldsymbol{L_d}$ of 5μm is considered.

V. COMPACT MODEL FOR SOA GAIN

The amplifier structure has been developed to be used in a monolithic InP active-passive integration platform. The goal is to obtain a compact model description of the SOA suitable for the design of photonic integrated circuits. This is done by measuring the modal gain $g\ (f, N)$ of the SOA and analyzing the results using a simplified analytical theory. This theory leads to a set of parameters that can be used to describe the modal gain and a relation between the current density and a scaled carrier density. An analysis is then applied using the rate equation for the carrier density to obtain a value for the scaling factor of the scaled carrier density. The scaling of the carrier density can then be checked by the study of the material transparency and the gain saturation of the SOA. The measurements are compared with the predicted behavior using the determined parameters from the unsaturated gain analysis. It is possible to obtain important parameters for single mode ridge amplifiers by fitting them to the measurement results of the unsaturated gain, optical saturation, and material transparency. The parameters representative of the SOA performance are the transparency carrier density N_0, the passive loss α, the injection efficiency η_i and the input saturation power $P_{in,sat}$.

In integrated photonics one want to use amplifiers and waveguides that operate on a single transverse mode and can at most have a lossy second mode [32]. It is well known that the smaller ridge widths needed for single mode operation in the amplifier leads to a reduction in its performance compared to broad area lasers [26]. As an example of this performance reduction, Fig. 6 shows the measured transparency current density as function of the ridge width. From the graph, it is noticeable how for single mode ridge widths, the transparency current is three times higher than for broad area stripes. This is due to the increase in the current leakage and in the effect of non-radiative carrier recombination [33]. Therefore, values of parameters such as the injection efficiency determined in the previous section cannot be used directly in the analysis of single mode ridge amplifiers.

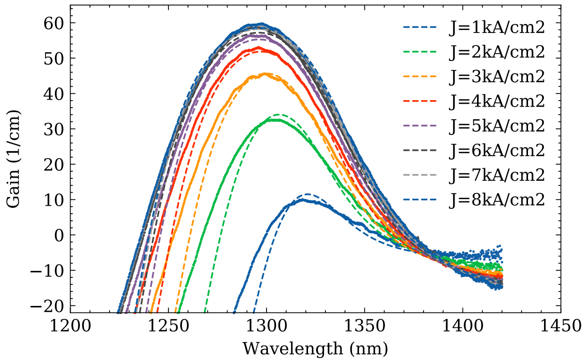

Fig. 7. Modal gain spectra from the fit of ASE measurements (dots) and calculated from the parametrized model (dashed) for different injected current densities.

A. Unsaturated Modal Gain

There are several ways the unsaturated modal gain of the optical amplifier can be measured. There are methods based on the contrast ratio of each cavity mode of the amplified spontaneous emission (ASE) [34]. However, this method is sensitive to the noise and to the measurement equipment resolution due to the small light intensity at the minimum. This has led researchers to study multiple electrodes methods. In this paper, the unsaturated gain spectra of the 1300 nm SOA are determined by the analysis of the ASE spectra from different amplifier lengths as described by Thompson *et al.* and Pustakhod *et al.* [35], [36]. The measurements of different amplifier stripes with different lengths are needed to reduce the effect of the coupling loss to the chip facets which are hard to control due to variations in the fabrication of optical waveguides. Averaging measurements with different SOA lengths and different coupling loss it is possible to link the gain and the ASE power density at each wavelength λ. To measure the unsaturated modal gain a series of shallowly etched ridge waveguide optical amplifiers, divided into two sections of different lengths, were processed on a single 2×2.5 mm^2 chip with anti-reflection (AR) coated facets. The two sections are addressed by different electrodes and are separated by 20 μm isolation sections where 1 μm of highest p doped top-cladding InP is removed to ensure electrical isolation between the two sections. One section is reversely biased to prevent any optical feedback into the amplifier to avoid unwanted laser operations, while the other one is being driven by current. The amplified spontaneous emission (ASE) spectra are detected using an optical spectrum analyzer connected to a lensed single mode output fiber. Automated alignment routines are performed to optimize the chip to fiber coupling as described in [37]. Multiple spectra from different amplifier lengths between 50 and 600 μm are measured. Measuring ASE from multiple SOA lengths allows us to identify some experimental points that deviate more than 10% from the overall averaged values. Those measurements were discarded in the fit, assuming that they derived from fabrication imperfections. In Fig. 7 the modal gain spectra for current densities between 1 and 8 kA/cm^2, are shown. A 3-dB gain bandwidth greater than 80nm is observed for a current density of J $=$ 5 kA/cm^2, together with a gain peak of 60 cm^{-1}. Having a wide bandwidth is of high importance in the realization of widely tunable laser systems, since the gain spectrum at the laser threshold is the ultimate limitation to the tuning range.

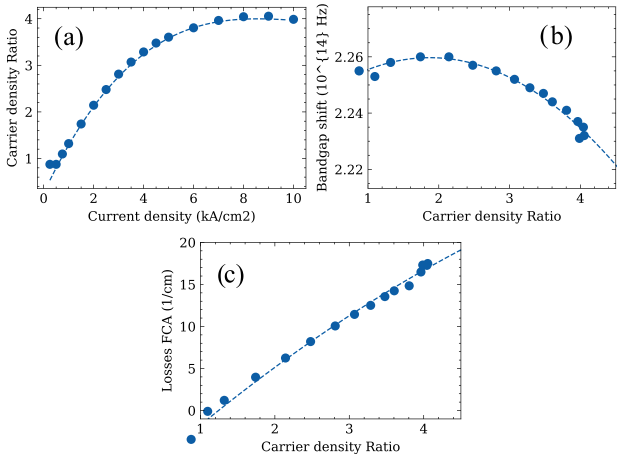

Fig. 8. (a) Carrier density ratio as function of injected current. (b) Frequency bandgap shift and (c) free carrier absorption losses as function of carrier density ratio. The dashed lines show polynomial parametrized fit of the dots.

The modal gain from a quantum well based SOA can be described using only few parameters using analytical approximations for the material gain. The model used here is derived by Balle [38]. Under the assumptions of parabolic energy bands and temperature equal to zero, the material gain spectrum g_{m} *(f, N)* as function of carrier density N inside the amplifier can be written as [38]:

$$g_m(f, N) = \chi \left[\operatorname{atan}\left(\frac{f - f_0(N)}{\gamma} \right) \right. \\ \left. - 2\operatorname{atan}\left(\frac{f - f_0(N)}{\gamma} - \frac{N}{N_0} \right) - \frac{\pi}{2} \right] \quad (1)$$

where $f_0(N)$ is the bandgap frequency which depends on the carrier density, γ is the homogenous line width, N_0 is the carrier density at transparency at the bandgap energy and χ is a gain scaling factor.

Hence the net modal gain g_{mod} will be:

$$g_{mod}(f, N) = \Gamma g_m(f, N) - \alpha(N) \quad (2)$$

where $\alpha(N)$ represents the amount of free carrier absorption losses inside the amplifier, due to the excitations of the light and heavy holes inside the valence band and Γ refers to the gain confinement factor in the quantum wells. The fit of the parameters in (1) and (2) to the experimental net modal gain spectra with, are depicted by the dashed lines in Fig. 7(b). Fig. 8(a), (b) and (c) show respectively the fitted values found for the scaled carrier density ratio $N_r = N/N_0$ as function of injection current density, the bandgap frequency shift, and the free carrier absorption losses as function of carrier density ratio.

The fit is obtained for all current densities with the same value for the homogenous linewidth $\gamma = 5.0$ THz, and a scaling factor of $\chi = 1050$ cm^{-1}. It is interesting to note that the values of γ and χ are near identical to those determined for 1550 nm quantum well amplifiers. The confinement factor of 4% for a single mode ridge width amplifier is calculated using PicWave software from Photon Design.

In Fig. 8(a), the carrier density increases with the injected current density, until it reaches its maximum at approximately 4 times the transparency carrier density value N_0. This suggests the presence of a carrier overshoot mechanisms, which arises from the fact that more injected carriers are recombining in the InP outside of the active region. In this way, the gain spectra remain constant for higher current densities. This can be improved either by increasing the number of the well in the active region, which will affect the SOA optical saturation, or by applying a graded index structure in the spatial confinement heterostructure to better confine the carriers inside the SOA active region. This can however create issues for the active passive integration reflection and mode overlap. Fig. 8(b) depicts the bandgap frequency shift f_0 as function of the carrier density inside the amplifier. The bandgap follows a square-root or a cubic-root dependence on the carrier density ratio as suggested by Tomita *et al.* [39] and Kleinman *et al.* [40]. In Fig. 8(c) the fitted values for the optical loss α as a function of the scaled carrier density are presented. The linear relation between the carrier density and losses indicates these are absorption losses due to the absorption of light from the holes present in the active region. The values found here are lower than those determined in 1550 nm InP quantum well-based amplifiers [38]. This indicates the higher efficiency of 1300 nm quantum wells amplifier with respect to C and L-band InP amplifiers. Fitted polynomial functions, as shown in Fig. 8(a), (b) and (c), can be used to parametrize these three single mode ridge width amplifier properties that will be used to model the SOA performance. Note that this parametrization underestimates the gain at higher energies, due to some approximations on which the model in [38] is based.

B. Amplifier Rate Equation and Carrier Density at Transparency

The relation between the current density and the scaled carrier density can be analyzed further to determine a value of N_0. For this purpose, the rate equation for the carrier density in an optical amplifier can be used.

The time evolution of the carrier density inside the active region of an optical amplifier is described by [41]:

$$\frac{dN}{dt} = -v_g g_{mat}(f,N)\,P + \frac{Jw\eta_i}{qS_{mode}\Gamma} - R\,(N) \qquad (3)$$

Where the first right hand side term describes the carrier depletion due to stimulated emission, the second one is the pump rate, which determines the number of carriers injected in the active region and the third one refers to possible recombination mechanisms. The second right hand side term, which corresponds to the pump rate, directly depends on the current density *J*, the ridge width *w* and the injection efficiency η_i and it is inversely proportional to the optical confinement Γ times the modal area S_{mode}. For the S_{mode} parameter, which is dependent on the geometry of the structure, the effective mode size [42] was used. This was calculated to be 1.63 um^2 using a commercial mode solver MODE from Lumerical Inc.

TABLE I

Coefficients in the Carrier Rate Equation

Coefficient	Value	Units
A [27]	$1.68\ 10^{-8}$	s^{-1}
B [27]	$2.6\ 10^{-10}$	$cm^3 s^{-1}$
C [43]	$1.417\ 10^{-28}$	$cm^6 s^{-1}$
D	$2.5\ 10^{-90}$	$cm^{13.5} s^{-1}$
$\boldsymbol{v_g}$	$0.83\ 10^{8}$	$m\ s^{-1}$
$\boldsymbol{S_{mode}}$	1.63	μm^2
$\boldsymbol{\Gamma}$	0.04	-
$\boldsymbol{\eta_i}$	0.65	-
$\boldsymbol{N_0}$	$0.575\ 10^{18}$	cm^{-3}

Assuming that the photon number inside the active region is negligible during the modal gain measurements which implies there is no significant carrier loss due to ASE, it is possible to set to zero the stimulated recombination term and (3) becomes:

$$\frac{dN}{dt} = \frac{\eta_i\ J\ w_r}{q\ S_{mode}\Gamma} - AN - BN^2 - CN^3 - DN^{5.5} \qquad (4)$$

Where the recombination processes are expressed as a polynomial function of the carrier density N. The A,B,C,D coefficients represent the probability to occur of each recombination mechanism [43], [44]. A, B, and C are extracted from [27] and [44], while D has been kept as a fitting parameter. At steady state conditions, under which the measurements were done, the carriers are at equilibrium and the rate equals zero. It is then possible to find solutions that link the carrier density inside the active region to the injected current density into the device. When we compare the solution of (4) with the carrier density ratio extracted from (1), it is possible to determine the transparency carrier density N_0, the injection efficiency η_i and the D term that corresponds to the carrier leakage inside the amplifier due to current drift as explained in [44]. Table I summarizes all the values that were used to obtain the solutions of (3) and (4).

The values of $\eta_i = 0.65$ and $N_0 = 0.575\ 10^{18}$ cm^{-3} , are calculated through the agreement between the two curves for current densities between 1 and 7 kA/cm^2. At higher injected current densities, the two curves start to slightly deviate from each other. The highest carrier dependence of the recombination mechanisms in (4) is referring to the leakage due to the carrier drift as explained in [31], but from the parametrization of the unsaturated gain measurements, it is evident that the carrier density is clamped at a maximum value of four times the carrier density at transparency for current densities of 7 kA/cm^2 and higher. This behavior indicates that inside the SOA, the injected carriers can easily escape from the low energy barriers and spatial confinement heterostructures (SCH). This limitation comes from a particular design choice for the active layers' epitaxial growth since the barriers were chosen to minimize reflections at the active passive butt-joint integration interfaces and not as an optimized energy barrier layer for the carriers escape.

The calculation of N_0 and η_i are verified through the measurements of material transparency and optical saturation. Measurements of the material transparency current density have been performed by recording the change in voltage over the SOA

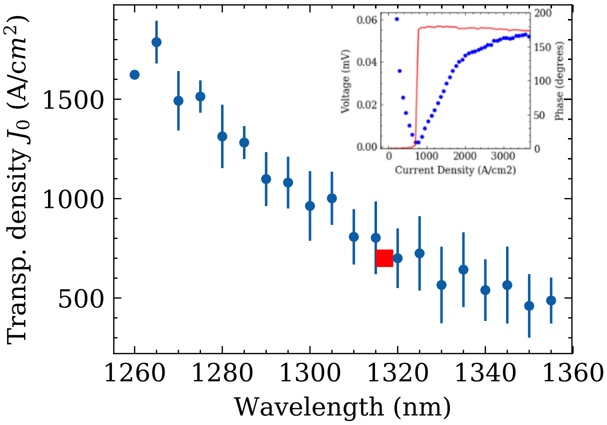

Fig. 9. Transparency current density as function of input laser wavelength (blue). Results are obtained from measurements of three different device lengths of 300, 560, and 1100 μm. The (red) dot is the transparency current density derived from the analysis with equation (4) of the unsaturated gain parametrized model. An example of a detected signal (inset) is shown where both the amplitude and the phase of the signal are detected.

induced by an external laser as function of current density. An external laser is on/off modulated at 300 kHz and coherent light at a particular frequency is injected into a 2 μm wide shallow etched ridge SOA. The current bias is swept over a range that includes the material transparency point and both the amplitude (mV) and the phase (degrees) of the voltage change over the amplifier are detected with the lock-in amplifier (LIA) as also described in [45]. For lower injection currents the amplifier is absorbing the external laser light, thus generating carriers and increasing conductivity which reduces the voltage over the diode structure. While for higher currents the quantum well material starts to provide gain which reduces the carrier concentration when the light is in the SOA, the conductivity is reduced and the voltage over the SOA increases. The minimum value in the amplitude of the voltage modulation corresponds to a π phase jump which means that the voltage modulation over the SOA is changing its electrical polarity. The current at which this transition occurs is described as the material transparency current at the input wavelength.

Fig. 9 shows the material transparency current density as function of the external laser wavelength. In the inset graph a measurement example is presented. Lower wavelengths present higher transparency current densities as suggested by the modal gain spectra on Fig. 7. The red dot in Fig. 9 is coming from the N_0 determination from the carrier density rate equation. J_0 is defined as the current density at transparency, which refers to the transparency carrier density N_0 at the bandgap frequency $f_0(N_0)$. The model predicts $J_0 =$ 707 A/cm^2 at 1317 nm, which agrees with the measurement of material transparency.

C. Optical Gain Saturation

When light enters the SOA with photon density $P \neq 0$, we need to introduce a second equation that describes the time evolution of the photon density inside the amplifier. In an optical amplifier the rate of photons generated through stimulated recombination can be expressed as:

$$\frac{dP}{dt} = v_g\ (f)\, g_{mod}\,(f, N)\, P\,(t)\,, \tag{5}$$

where v_g is the group velocity g_{mod} is the modal gain of (2) and P is the photon density at a time *t*. In a one-dimensional device, the signal power P in the SOA is determined from the travelling-wave equation [46] as:

$$\frac{dP}{dx} = g_{mod}\ P. \tag{6}$$

Applying a fixed current and fixed input optical power at a single wavelength λ, it is possible to obtain the output photon number of an amplifier as function of injected current and length of the device. This is done by solving the system of coupled differential (3) and (5) at the steady state condition (i.e., dN/dt $= 0$ and $dP/dt = 0$), using the Runge-Kutta method [47]. Thus, it is possible to determine amplification $G\ = P_{out}\ / P_{in}$, for a particular photon frequency and injection current density. The calculated gain decreases as function of input power due to the significant increase of the carrier depletion inside the active region. This mechanism leads to the optical gain saturation of the SOA. The input saturation power is identified as the input power for which the amplifier gain drops to half of its value and it is linked to the maximum output power by Davenport [48]:

$$P_{in,sat} = \frac{P_{out,max}}{G_0 - 2} \tag{7}$$

where G_0 is the unsaturated linear amplification and $P_{out,max}$ is the output saturation power. It is important to state that the saturation power is dependent on current, wavelength and amplifier length.

To determine the saturation input power levels and to check the prediction of the gain saturation using the measured unsaturated gain data and the extracted carrier density values, the optical saturation of a series of shallowly etched ridge waveguide optical amplifiers was measured. These were special devices where the waveguide on the chip was divided into two sections of different length. The two sections are addressed by different electrodes and are separated by 20 μm electrical isolation sections where 1 μm of top cladding highly p doped InP is removed to ensure electrical isolation between the two sections. The first section, where the laser light enters, is operated as an SOA. The second section is reversely biased to detect the light amplified by the first section. A reverse bias voltage of -1V is applied to the second section amplifier to increase the detector absorption. Since the resistance of the isolation section is lower than 1 k Ω , it becomes possible to extend the carrier detection area to the isolation section. Thus, the light absorbed in the isolation section is included in the signal measured at the detector. The reference input power is obtained by shorting the two electrodes at the same reverse bias V_b and extracting the amplifier photocurrent with the LIA as function of input power from a modulated external laser with different attenuation settings. The opportunity to use an integrated solution for light amplification and detection can lead to the full on-chip characterization of the amplifier optical properties [49]. The devices were processed on a single 2×2.5 mm^2 chip with anti-reflection (AR) coated facets.

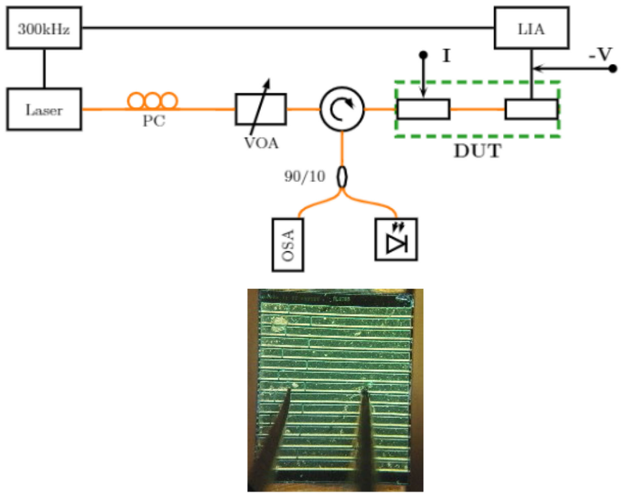

Fig. 10. Setup schematics and microscope image of the device under test (DUT). Variable optical attenuator (VOA), lock-in amplifier (LIA) and optical spectrum analyzer (OSA).

The experimental setup used to characterize the optical amplifiers is shown in Fig. 10. When the first section optical amplifier is driven with forward bias and no light is injected from an external source, it is possible to perform automated alignment through the maximization of the power reading from an external detector (Agilent81636B) [37] and read the current dependent ASE from an optical spectrum analyzer (OSA) (ANDO AQ6315A). When we inject an on/off modulated (300kHz) TE polarized light from a tunable laser source (Santec TSL-520) into the amplifier, the second amplifier section is used as a detector. The first section amplification is detected as function of input laser power, which is controlled through a variable optical attenuator (VOA). This is done after a polarization controller (PC), used to optimize the polarization of the input light to TE. A LIA (Stanford SR865A) is connected to the photodetector section to increase the sensitivity of the measurements and avoid any effect from the current leakage or the electrical crosstalk between the two SOA segments. In Fig. 10, it is possible to see how the device under test (DUT) looks like under an optical microscope, when the two sections are probed.

The device temperature is stabilized to 20 °C with a temperature-controlled copper mount. The optical gain saturation measurements are performed to verify the evaluation of the injection efficiency parameter η_i inside the optical amplifier model. The first section amplifier is biased with current densities J between 2 and 7 kA/cm^2. The lower current density limit is chosen to ensure a current density above material transparency for every wavelength inside the 1300 nm region and the upper limit is decided to be 7kA/c m^2. The upper current density limit has been chosen as the one that ensures matching between the carrier density obtained from the gain parametrization with (1) and the solution of the amplifier rate equation with (4).

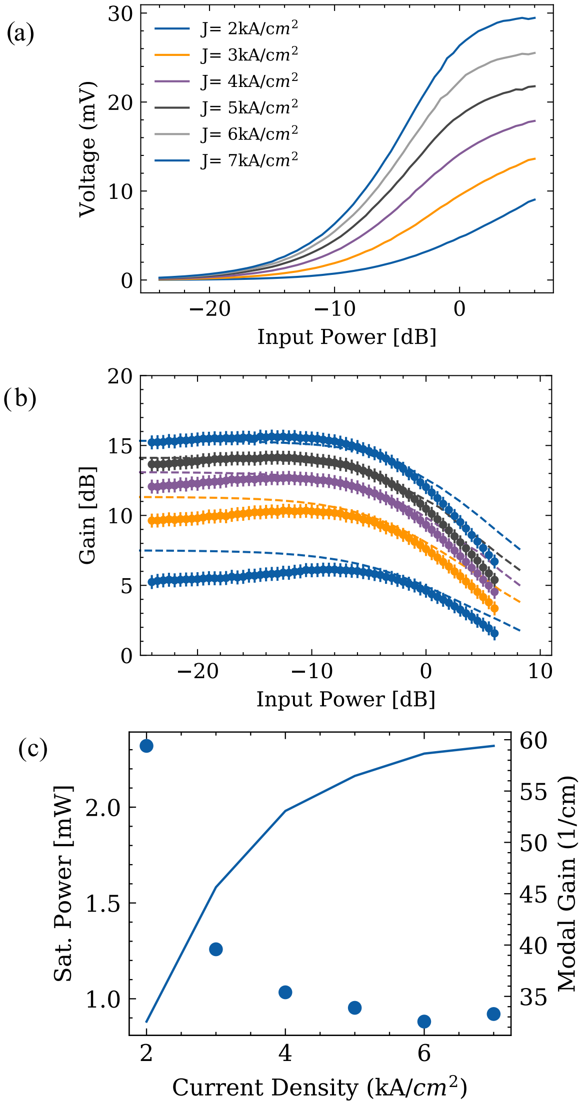

Fig. 11. (a) Measured signal on the detector at different current density (b) Measured gain saturation (dotted) and predictions based on the parametrized model (dashed). (c) saturation input power and small signal gain as function of current density. Measurements performed on a 600 μm long SOA with laser ligth at 1300 nm. Legend in (a) is valid in all plots.

Fig. 11(a) shows an example of a measurement results for a 600 μm long SOA for different currents as function of external laser power at a particular wavelength $\lambda\ =\ 1300\ $nm. The detector voltage as function of optical input power clearly shows for high optical power the presence of optical gain saturation. Fig. 11(b) shows the amplifier gain as function of the laser power in a logarithmic plot. The dashed line represents the optical gain saturation predicted by the model. The error bars of ± 0.5 dB in the measurement points represent the error due to the uncertainty on the coupling loss due to variations in the fiber to waveguide alignment, which can be between 3 and 4 dB. The deviation of the measurement curves with the model prediction are an artifact due to the dynamic range of the LIA. Since the LIA input range is maximized to the highest value obtained at high input photon density, at low input power its sensitivity is decreased and in this way it underestimates the ratio of the output power with respect to input power. This also explains why before saturation, the small signal gain increases instead of slightly decreasing with the increase in optical power. This artifact is more prominent at low injected current densities since the optical amplification is lower. From the gain curves is

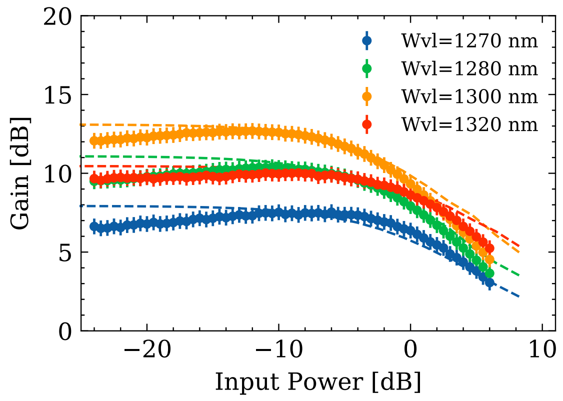

Fig. 12. Optical gain saturation measurements (dotted) and model (dashed) at 4 kA/cm^2 for different input laser wavelengths.

possible to extract the $P_{in,sat}$ from [48] as in Fig. 11(c). It is identified as the input power when the gain decreases to half of its unsaturated value G_0, i.e when any increase in the opticalinput power does not produce any increase in the output power from the SOA. From Fig. 11(c), it is visible how the input saturation power decreases with current density. It varies between 2 and 0.5 mW for a 600 um long SOA. This lead to approximately 30 mW maximum output power at 1300 nm for a 600 um long SOA with 7 kA/cm^2 injected current.

In Fig. 12 the gain saturation curves are plotted as function of wavelength for the same device length and an injected current of 4 kA/cm^2. It is shown how the highest gain is at the center of the gain spectrum for that particular current. Moreover, for wavelength closer to the modal gain maximum the gain is higher but at the same time $P_{in,sat}$ is lower, keeping an approximately constant maximum optical power with wavelength for the same current density. The optical saturation predicted by the model (dashed line) can be used to predict the amplifier gain behavior as function of input wavelength as well as for different SOA lengths.

VI. CONCLUSION

In this work, we have designed, fabricated, and characterized a new 1.3 μm InGaAsP/InP semiconductor optical amplifier that is optimize for a monolithic active/passive generic integration technology. This SOA is compatible with a butt-joint integration scheme with low active/passive interface reflections, and it shows high performance in terms of efficiency ($\eta_i = 0.82$) and temperature dependence compared to what available in literature. The layer stack design is optimized in terms of thickness and compressive strain of the quantum well to ensure maximized overlap with a bulk low loss passive waveguide on InP. Fabry-Perot laser measurements reveal output power levels as high as 2.5 W and characteristic temperatures as good as 75 K. A self-consistent compact model for the description of ridge width amplifier has been described and validated. The analysis indicates a reduced free carrier absorption loss compared to 1550 nm InP based SOAs, a gain bandwidth as broad as 80 nm, limited by the carrier density, and a higher than 30 mW output saturation power from single mode ridge waveguide amplifier 600 um long in saturation. Therefore, this building block contributes to the development of an InP monolithic integration technology in the 1300 nm range, which can be utilized for the development of photonic integrated circuits for data communication and biomedical imaging and other applications.

REFERENCES

[1] M. Hoppe *et al.*, “High speed external cavity diode laser concept based on a resonantly driven MEMS scanner for the mid-infrared region,” *Appl. Opt.*, vol. 60, no. 15, pp. C92–C97, 2021, doi: 10.1364/ao.420041.

[2] B. Mason, J. Barton, G. A. Fish, L. A. Coldren, and S. P. DenBaars, “Design of sampled grating DBR lasers with integrated semiconductor optical amplifiers,” *IEEE Photon. Technol. Lett.*, vol. 12, no. 7, pp. 762–764, Jul. 2000, doi: 10.1109/68.853492.

[3] L. A. Coldren, G. A. Fish, Y. Akulova, J. S. Barton, L. Johansson, and C. W. Coldren, “Tunable semiconductor lasers: A tutorial,” *J. Lightw. Technol.*, vol. 22, no. 1, pp. 193–202, Jan. 2004, doi: 10.1109/JLT.2003.822207.

[4] P. J. A. Thijs, T. Van Dongen, L. F. Tiemeijer, and J. J. M. Binsma, “Strained-layer quantum well lasers,” *IEEE J. Light. Technol.*, vol. 12, no. 1, 1994.

[5] J. Jin, D. Tian, J. Shi, and T. Li, “Fabrication and complete characterization of polarization insensitive 1310 nm InGaAsP-InP quantum-well semiconductor optical amplifiers,” *Semicond. Sci. Technol.*, vol. 19, no. 1, pp. 120–126, 2003, doi: 10.1088/0268-1242/19/1/020.

[6] A. Ferrari *et al.*, “Assessment on the achievable throughput of multi-band ITU-T G.652.D fiber transmission systems,” *J. Lightw. Technol.*, vol. 38, no. 16, pp. 4279–4291, Aug. 2020, doi: 10.1109/JLT.2020.2989620.

[7] Ł. Chorchos and J. P. Turkiewicz, “Performance comparison of the 1310 nm optical amplifiers,” *Photon. Appl. Astron. Commun. Ind. High-Energy Phys. Exp.*, vol. 10031, 2016, Art. no. 100311C, doi: 10.1117/12.2249337.

[8] D. A. Ackerman *et al.*, “Analysis of gain in determining T 0 in 1.3 μm semiconductor lasers,” *IEEE J. Sel. Top. Quantum Electron.*, vol. 1, no. 2, pp. 250–263, Jun. 1995, doi: 10.1109/2944.401204.

[9] L. F. Tiemeijer *et al.*, “High-gain 1310 nm semiconductor optical amplifier modules with a built-in amplified signal monitor for optical gain control,” *IEEE Photon. Technol. Lett.*, vol. 9, no. 3, pp. 309–311, Mar. 1997, doi: 10.1109/68.556056.

[10] P. J. A. Thijs, L. F. Tiemeijer, J. J. M. Binsma, and T. van Dongen, “Progress in long-wavelength strained-layer InGaAs (P) quantum-well semiconductor lasers and amplifiers,” *IEEE J. Quantum Electron.*, vol. 30, no. 2, pp. 477–499, Feb. 1994, doi: 10.1109/3.283797.

[11] T. Higashi, T. Yamamoto, S. Ogita, and M. Kobayashi, “Experimental analysis of characteristic temperature in quantum-well semiconductor lasers,” *IEEE J. Sel. Top. Quantum Electron.*, vol. 3, no. 2, pp. 513–521, Apr. 1997, doi: 10.1109/2944.605702.

[12] A. Fiore, C. Zinoni, B. Alloing, V. Zwiller, L. H. Li, and C. Monat, “Nanoscale single quantum dot devices at 1300 nm,” *Quantum Dots, Nanoparticles, Nanoclusters II*, vol. 5734, pp. 106–115, 2005, doi: 10.1117/12.598039.

[13] S. Latkowski *et al.*, “Monolithically integrated 25 GHz extended cavity mode-locked ring laser with intracavity phase modulators,” *Opt. Lett.*, vol. 40, no. 1, pp. 77–80, 2015, doi: 10.1364/ol.40.000077.

[14] I. M. Soganci *et al.*, “Monolithically integrated InP 1 × 16 optical switch with wavelength-insensitive operation,” *IEEE Photon. Technol. Lett.*, vol. 22, no. 3, pp. 143–145, Feb. 2010, doi: 10.1109/LPT.2009.2036859.

[15] P. Dong *et al.*, “Novel integration technique for silicon/III-V hybrid laser,” *Opt. Exp.*, vol. 22, no. 22, pp. 26854–26861, 2014, doi: 10.1364/oe.22.026854.

[16] A. Y. Liu and J. Bowers, “Photonic integration with epitaxial III-V on silicon,” *IEEE J. Sel. Top. Quantum Electron.*, vol. 24, no. 6, pp. 1–12, Nov./Dec. 2018, Art. no. 6000412, doi: 10.1109/JSTQE.2018.2854542.

[17] L. M. M. I. T. Chen Siming *et al.*, “InAs /GaAs quantum dot lasers monolithically grown on on-axis si (001) substrates,” *Opt. Exp.*, vol. 25, no. 5, pp. 11381–11386, 2017.

[18] S. Liu and A. Khope, “Latest advances in high-performance light sources and optical amplifiers on silicon,” *J. Semicond.*, vol. 42, no. 4, 2021, Art. no. 041307, doi: 10.1088/1674-4926/42/4/041307.

[19] M. Buffolo *et al.*, “Degradation mechanisms of heterogeneous III-V/Silicon 1.55- μm DBR laser diodes,” *IEEE J. Quantum Electron.*, vol. 53, no. 4, pp. 1–8, Aug. 2017, Art. no. 8400108, doi: 10.1109/JQE.2017.2714582.

[20] D. D'Agostino *et al.*, "Low-loss passive waveguides in a generic InP foundry process via local diffusion of zinc," *Opt. Exp.*, vol. 23, no. 19, 2015, Art. no. 25143, doi: 10.1364/oe.23.025143.

[21] A. Meighan, Y. Yao, M. J. Wale, and K. A. Williams, "Design of 100 GHz-class Mach-Zehnder modulators in a generic indium phosphide platform," in *Proc. IEEE Photon. Conf.*, 2020, pp. 1–2, doi: 10.1109/IPC47351.2020.9252410.

[22] L. M. Augustin *et al.*, "InP-based generic foundry platform for photonic integrated circuits," *IEEE J. Sel. Top. Quantum Electron.*, vol. 24, no. 1, pp. 1–10, Jan./Feb. 2018, Art. no. 6100210, doi: 10.1109/JSTQE.2017.2720967.

[23] A. D. Andreev and D. V. Donetsky, "Analysis of temperature dependence of the algaassb quantum-well lasers," *Appl. Phys. Lett.*, vol. 2743, pp. 8–11, 1999.

[24] D. P. Sapkota, M. S. Kayastha, and K. Wakita, "Dependence of threshold current density on quantum well composition for compressive strained-layer alxgayin1-x-yas lasers," in *Proc. Conf. Int. Conf. Indium Phosphide Relat. Mater.*, 2010, pp. 261–264, doi: 10.1109/ICIPRM.2010.5516084.

[25] M. A. Reshchikov, "Measurement and analysis of photoluminescence in gaN," *J. Appl. Phys.*, vol. 129, no. 12, 2021, Art. no. 121101, doi: 10.1063/5.0041608.

[26] K. S. Mobarhan, "Test and characterization of laser diodes: Determination of principal paramters," Newport Appl. Note, no. 1, pp. 1–7, 2006.

[27] L. A. Coldren, "Diode lasers and photonic integrated circuits," *Opt. Eng.*, vol. 36, no. 2, 1997, Art. no. 616, doi: 10.1117/1.601191.

[28] H. Park, P. Srinivasan, M. L. Davenport, M. N. Sysak, and R. Jones, "Experimental investigations of characteristic temperatures of hybrid silicon lasers," *IEEE J. Quantum Electron.*, vol. 48, no. 12, pp. 1512–1518, Dec. 2012, doi: 10.1109/JQE.2012.2222870.

[29] T. Tsuchiya, D. Takemoto, T. Sudou, and M. Aoki, "Low-threshold and high-temperature characteristics of 1.3-/spl mu/m InGaAlAs MQW lasers grown by metalorganic vapor-phase epitaxy," in *Proc. Int. Conf. Indium Phosphide Related Mater*, 2000, pp. 266–269.

[30] J. Piprek, P. Abraham, and J. E. Bowers, "Cavity length effects on internal loss and quantum efficiency of multiquantum-well lasers," *IEEE J. Sel. Top. Quantum Electron.*, vol. 5, no. 3, pp. 643–647, May/Jun. 1999, doi: 10.1109/2944.788430.

[31] T. Cho, H. Kim, Y. Kwon, and S. Hong, "Theoretical study on intervalence band absorption in InP-based quantum-well laser structures," *Appl. Phys. Lett.*, vol. 68, no. 16, pp. 2183–2185, 1996, doi: 10.1063/1.116006.

[32] M. Smit *et al.*, "An introduction to InP-based generic integration technology," *Semicond. Sci. Technol.*, vol. 29, no. 8, 2014, Art. no. 083001, doi: 10.1088/0268-1242/29/8/083001.

[33] V. Swaminathan, J. M. Freund, L. M. F. Chirovsky, T. D. Harris, N. A. Kuebler, and L. A. D'Asaro, "Evidence for surface recombination at mesa sidewalls of self-electro-optic effect devices," *J. Appl. Phys.*, vol. 68, no. 8, pp. 4116–4118, 1990, doi: 10.1063/1.346252.

[34] Y. Barbarin *et al.*, "Gain measurements of Fabry-Perot InP/InGaAsP lasers using an ultrahigh-resolution spectrometer," *Appl. Opt.*, vol. 45, no. 35, pp. 9007–9012, 2006, doi: 10.1364/AO.45.009007.

[35] D. Pustakhod, K. Williams, and X. Leijtens, "Fast and robust method for measuring semiconductor optical amplifier gain," *IEEE J. Sel. Top. Quantum Electron.*, vol. 24, no. 1, pp. 1–9, Jan./Feb. 2018, Art. no. 3100309.

[36] J. D. Thomson, H. D. Summers, P. J. Hulyer, P. M. Smowton, and P. Blood, "Determination of single-pass optical gain and internal loss using a multisection device," *Appl. Phys. Lett.*, vol. 75, no. 17, pp. 2527–2529, 1999, doi: 10.1063/1.125066.

[37] S. Latkowski, D. Pustakhod, M. Chatzimichailidis, W. Yao, and X. J. M. Leijtens, "Open standards for automation of testing of photonic integrated circuits," *IEEE J. Sel. Top. Quantum Electron.*, vol. 25, no. 5, pp. 1–8, Sep./Oct. 2019, Art. no. 6100608, doi: 10.1109/JSTQE.2019.2921401.

[38] S. Balle, "Simple analytical approximations for the gain and refractive index spectra in quantum-well lasers," *Asian J. Chem.*, vol. 23, no. 10, pp. 4397–4399, 2011.

[39] A. Tomita and A. Suzuki, "Carrier-induced lasing wavelength shift for quantum well laser diodes," *IEEE J. Quantum Electron.*, vol. QE-23, no. 7, pp. 1155–1159, Jul. 1987, doi: 10.1109/JQE.1987.1073481.

[40] D. A. Kleinman and R. C. Miller, "Band-gap renormalization in semiconductor quantum wells containing carriers," *Phys. Rev. B*, vol. 32, no. 4, pp. 2266–2272, 1985, doi: 10.1103/PhysRevB.32.2266.

[41] C. Miller, "Laser rate equations," *Physics*, 2008.

[42] R. Paschotta, "Article on 'effective mode area'," in *Encyclopedia of Laser Physics and Technology*. Weinheim, Germany: Wiley-VCH, 2008.

[43] M. E. Prise, M. R. Taghizadeh, S. D. Smith, and B. S. Wherrett, "Picosecond measurement of auger recombination rates in InGaAs," *Appl. Phys. Lett.*, vol. 45, no. 6, pp. 652–654, 1984, doi: 10.1063/1.95344.

[44] M. Kot and K. Zdansky, "Measurement of radiative and nonradiative recombination rate in InGaAsP-InP LED's," *IEEE J. Quantum Electron.*, vol. 28, no. 8, pp. 1746–1750, Aug. 1992, doi: 10.1109/3.142567.

[45] G. Pakulski *et al.*, "Transparency current density of gainnas lasers," *Photon. North Opt. Compon. Devices*, vol. 5577, pp. 82–87, 2004, doi: 10.1117/12.567550.

[46] M. J. Connelly, "Optical amplifiers: SOAs," *Encycl. Mod. Opt.*, vol. 1–5, pp. 242–254, 2018, doi: 10.1016/B978-0-12-803581-8.09462-5.

[47] J. C. Butcher, "A history of Runge-Kutta methods," *Appl. Numer. Math.*, vol. 20, pp. 247–260, 1996.

[48] M. L. Davenport, S. Skendzic, N. Volet, J. C. Hulme, M. J. R. Heck, and J. E. Bowers, "Heterogeneous silicon/III-V semiconductor optical amplifiers," *IEEE J. Sel. Top. Quantum Electron.*, vol. 22, no. 6, pp. 78–88, Nov./Dec. 2016, doi: 10.1109/JSTQE.2016.2593103.

[49] J. Hazan, K. A. Williams, and E. A. J. M. Bente, "Gain spectra and saturation power measurements in a two-section InGaAsP /InP semiconductor optical amplifier at 1.3 μm," in *Proc. IEEE Photon. Benelux Symp.*, 2021, Paper 4.